A numerical study on dust devils with implications to global dust budget estimates

Martina Klose *, Yaping Shao

Institute for Geophysics and Meteorology, University of Cologne, Pohligstr. 3, 50969 Cologne, Germany

ARTICLE INFO

ABSTRACT

The estimates of the contribution of dust devils (DDs) to the global dust budget have large uncertainties because the dust emission mechanisms in DDs are not yet well understood. In this study, a large-eddy simulation model coupled with a dust scheme is used to investigate DD dust entrainment. DDs are identified from the simulations using various threshold values for pressure drop and vorticity in the DD center. A vortex-tracking algorithm is presented, which automatically detects and tracks vortices based on different pressure drop and vorticity criteria. The results show that DD dust lifting can be largely explained by convective turbulent dust emission. DD dust entrainment varies strongly between individual DDs even for similar atmospheric conditions, but the maximum emissions are determined by atmospheric stability. By relating DD emission and counts to the Richardson number, we propose a new and simple method to estimate regional and global DD dust transport.

© 2016 Elsevier B.V. All rights reserved.

1. Introduction

Dust devils (DDs) are small dust carrying vortices. They occur frequently on Earth and Mars, but their contributions to the terrestrial and martian dust budget are so far not well quantified. DDs are subgrid systems in global models and it is not clear how DD dust emission can be parameterized. Renno et al. (1998) developed a thermodynamic theory for DD occurrence and intensity, and based on this theory, Koch and Renno (2005) estimated the contribution of DDs to the terrestrial dust budget to be $\sim 26 \pm 18\%$. In their estimate, DD dust fluxes are determined from the maximum dust concentration and vertical wind speed measured in a small number of strong DDs. The resulting dust fluxes are not necessarily the surface dust fluxes and may lead to an overestimation of the DD dust contribution. Jemmett-Smith et al. (2015) used meteorological criteria to estimate the potential of DD occurrence, and found a much lower global DD contribution of 3.4% (estimates range from 0.9 to 31% depending on the criteria used). To obtain this estimate, Jemmett-Smith et al. (2015) used the same fractional updraft areas and dust fluxes as Koch and Renno (2005).

Dust emission mechanisms in DDs are subject to ongoing research. Saltation bombardment, the process in which dust emission is generated by impacts of hopping sand-sized grains, does not

alone explain dust emission in DDs, as the necessary condition to initiate saltation (i.e. the friction velocity, u_*, must be larger than the threshold friction velocity for saltation, u_{*t}) is often not reached. Other mechanisms specific to DD dust emission have been suggested, such as dust uplift due to a vertical pressure drop at the surface (suction), but the significance of this process has not yet been quantitatively determined (Balme and Hagermann, 2006). Also, the vertical pressure drop may be related to the tangential vortex speed, thus the consideration of vortex velocity may be sufficient in the study of DDs (Wang, 2016). As pressure drop is easier to measure than tangential vortex speed, it is often used as a direct indicator for DD intensity and DD dust load (e.g. Neakrase and Greeley, 2010; Metzger et al., 2011; Lorenz and Jackson, 2015).

Klose and Shao (2012) and Klose et al. (2014) have developed a parameterization for the direct aerodynamic dust entrainment by turbulence. The scheme focuses on convective conditions, the situation when DDs develop, and takes account of the stochastic nature of both atmospheric particle lifting forces and surface interparticle cohesive forces.

Large-eddy simulation (LES) is a powerful tool to investigate DDs (e.g. Deardorff, 1970; Kanak, 2005; Zhao et al., 2004; Gu et al., 2008), but apart from few exceptions (Michaels, 2006; Ito et al., 2010), DD dust entrainment has not been included in large-eddy simulation models. In this study, we use the Weather Research and Forecasting (WRF) model in LES mode coupled with the dust emission scheme of Klose et al. (2014) (KS14), denoted as WRF/LES-D (Klose and Shao, 2013). WRF/LES-D contains

---

* Corresponding author. Present address: USDA-ARS Jornada Experimental Range, P.O. Box 30003, MSC3 JER, NMSU, Las Cruces, NM88003, USA.
 E-mail address: mklose@nmsu.edu (M. Klose).

representations of dust emission, transport and deposition. The model is used to investigate DD occurrence, vortex properties, and dust emission for various atmospheric background conditions. By comparing the vortex properties and dust emission fluxes of the individual DDs detected in the LES runs, a new method is proposed to estimate large-scale DD dust transport from regional and global model data.

2. LES experiments

The numerical experiments are set up as described in Klose and Shao (2013). The model is run for various conditions of thermal stability and background wind. Stability is varied by setting different surface heat fluxes, H, for stable, neutral, and unstable stratifications ($H = -50, 0, 200, 400, 600 \, \text{Wm}^{-2}$). The background wind is initialized with a logarithmic wind profile determined by $u_* = 0.15, 0.3$, and $0.5 \, \text{m s}^{-1}$ and a surface roughness length of $z_0 = 0.01 \, \text{m}$, but the flow is allowed to freely develop during the model spin-up. A Rayleigh damping is applied to the top 300 m of the model domain to suppress gravity waves. In total, 15 numerical experiments (Table 1) are conducted for a $2 \times 2 \times 1.5 \, \text{km}^3$ domain (x×y×z) with a horizontal resolution of $\Delta x = \Delta y = 10 \, \text{m}$ and a vertical resolution which decreases with height. Assuming that the maximum size of large eddies in a convective boundary layer is comparable to the boundary layer depth, our domain can cover about four of the largest convective cells. This is at the lower limit for LES and a limitation for the experiments to allow for sufficient interaction between the strong convective cells (Schmidt and Schumann, 1989; Moeng and Sullivan, 2015). The simulated flow patterns show reasonable results, however, and we consider the domain size large enough for the purpose of this study. With a horizontal resolution of 10 m, the smallest detectable DDs have horizontal extents of $\sim 20{-}40 \, \text{m}$ (2–4 times Δx). This may lead to an underestimation of the number of small DDs in our study. The computational time step used in the simulations is 0.05 s and the output time step is 10 s. The simulation time for each experiment is 90 min, of which the first 30 min are used for model spin-up and are excluded from the analysis. The surface is specified as a loam soil.

The convective turbulent dust emission (CTDE) scheme of KS14 accounts for the stochastic nature of both atmospheric turbulence and inter-particle cohesion. In the scheme, the dust emission flux, F_D, for a given lifting force, f, and cohesive force, f_i, is given by

$$F_D = \begin{cases} \frac{\gamma_N}{2D} \left\{ -w_t m_p + T_p \left(f - f_i \frac{d_p}{D} \right) \right\} & \text{for } f > f_t, \\ 0 & \text{else} \end{cases} \quad (1)$$

Table 1
Surface heat flux H [W m^{-2}] and friction velocity u_* [m s^{-1}] used to initiate the LES experiments (Klose and Shao, 2013).

	H	u_*
Exp1	−50	0.15
Exp2	−50	0.3
Exp3	−50	0.5
Exp4	0	0.15
Exp5	0	0.3
Exp6	0	0.5
Exp7	200	0.15
Exp8	200	0.3
Exp9	200	0.5
Exp10	400	0.15
Exp11	400	0.3
Exp12	400	0.5
Exp13	600	0.15
Exp14	600	0.3
Exp15	600	0.5

with particle response time T_p, particle diameter d_p, viscous sub-layer thickness D, particle mass m_p, and particle terminal velocity w_t. $f_t = f_i + m_p g$ is the particle retarding force with g being gravitational acceleration. The dust emission flux for a given particle size d_j can be calculated as

$$F_{D,j} = \int_0^f F_D \cdot p_j(f_i) \mathrm{d}f_i \quad (2)$$

In the scheme's setup for use in meso- and large-scale models, f is parameterized to follow a probability distribution. In LES, the lifting force can be directly calculated from the model-resolved and subgrid-scale momentum fluxes as $f = \tau_f \pi d^2/4$ with

$$\tau_f = \rho \sqrt{\left(uw + \frac{1}{\rho} \tau_{sg,x} \right)^2 + \left(vw + \frac{1}{\rho} \tau_{sg,y} \right)^2} \quad (3)$$

where ρ is air density, u, v, and w are the resolved wind speed components respectively in x, y, and z direction, and $\tau_{sg,x}$ and $\tau_{sg,y}$ the components of subgrid-scale momentum flux in x and y direction. The scheme is an upgraded version from that used by Klose and Shao (2013) and has been calibrated against field observations. To the best of our knowledge, these are the first LES experiments including size-resolved DD dust entrainment.

3. Dust devil identification and tracking

DDs exhibit a characteristic pressure drop, Δp, and a maximum of vorticity, ζ, in the center (Sinclair, 1973; Renno et al., 1998). Vortex centers can be identified based on three criteria: (1) a local pressure minimum and vorticity maximum; (2) Δp exceeding a threshold Δp_t; and (3) ζ exceeding a threshold ζ_t (Ohno and Takemi, 2010; Raasch and Franke, 2011). Different threshold values have been proposed in the earlier studies. For example, Raasch and Franke (2011) defined Δp as the pressure perturbation from a base state at the lowest model level ($\sim 1 \, \text{m}$) and set $\Delta p_t = 0.04 \, \text{hPa}$ and $\zeta_t = 1 \, \text{s}^{-1}$. Ohno and Takemi (2010) used the pressure deviation from the horizontal domain average at 10 m height with $\Delta p_t = 0.1 \, \text{hPa}$ and $\zeta_t = 0.15 \, \text{s}^{-1}$.

For a 4 km^2 domain as used in this study, we consider the horizontal domain average pressure as a preferred reference and define Δp as the deviation of pressure from this average. Vorticity at grid point (i,j) is calculated as

$$\zeta(i,j) = \frac{2}{3} \left(\frac{v'(i+1,j) - v'(i-1,j)}{2\Delta x} - \frac{u'(i,j+1) - u'(i,j-1)}{2\Delta y} \right)$$
$$+ \frac{1}{3} \left(\frac{v'(i+2,j) - v'(i-2,j)}{4\Delta x} - \frac{u'(i,j+2) - u'(i,j-2)}{4\Delta y} \right). \quad (4)$$

where $u' = u - \overline{u}$ is the derivation of the wind component in x-direction from its horizontal domain average, and v' that in y-direction. The use of a weighted centered-difference approach increases the robustness for the computation of ζ. Different combinations of $\Delta p_t = 0.05, 0.1, 0.2$, and 0.25 hPa with $\zeta_t = 0.1, 0.2, 0.5$, and $1 \, \text{s}^{-1}$ are tested for the two meteorological standard heights 2 m and 10 m to investigate the sensitivity of the results to the choice of the identification criteria.

DD motion is tracked by estimating the expected position of the DD center at the following output time step, $(i,j)_{t+\Delta t}$, based on the mean wind. If a DD center is identified within the adjacent 7 grid points (70 m) of $(i,j)_{t+\Delta t}$ in any direction, i.e. within $(i \pm 7, j \pm 7)_{t+\Delta t}$, then both records are assumed to belong to the same track. The limit of 7 grid points is between about 0.5 and 3 times the DD translation distance per output timestep in the different wind settings as estimated from the average and standard deviation of wind speed at 10 m height and the DD positions.

Finally, the tracks are post processed to remove gaps arising from values of Δp and ζ which intermittently fail to meet the threshold criteria. If a DD track ends, but a new track begins within 7 grid points around $(i,j)_{t+m\Delta t}$, with $1 < m < 3$, and the intermediate locations exhibit local pressure minima, then the two tracks are connected. Tracks with durations shorter than 30 s are excluded.

4. Number of dust devils

Fig. 1 shows the number density of DDs

$$n = \frac{N}{AT} \qquad (5)$$

for 10 m height, where N is the number of DDs detected in area A during time period T. DDs are only detected in the experiments with unstable stratifications (Exp7–15, Table 1), except for one case in Exp6, which satisfies the weakest threshold requirements (one case in Exp1 for the 2 m level). These outliers are not included in the analyses. Most DDs are detected in the situations of strong thermal instability and weak wind shear (e.g. Exp13). The results for the 2 and 10 m levels are qualitatively consistent, but n is larger at 10 m. For a given height, n decreases with increasing Δp_t approximately exponentially (Kurgansky, 2006; Lorenz, 2012; Lorenz, 2014). Changes in ζ_t affect n only if Δp_t is small. For larger Δp_t, detected DDs have sufficiently large vorticity to exceed even the stricter ζ_t thresholds (see also Fig. 4a). A table listing n for Exp7-15, obtained using the different identification thresholds, is provided as Supplementary material.

Richardson number, Ri, is a measure for atmospheric stability accounting for both buoyancy and wind shear (Richardson, 1920) and is thus a suitable quantity to use for estimating DD occurrence. We calculate Ri following Businger et al. (1971). Unless otherwise noted, figures and equations in the remainder of this paper refer to Ri calculated for 10 m height. A decrease of n with Ri^2 for negative Ri is found (Fig. 2a):

$$n = \beta Ri^2 \qquad (\text{with } Ri < 0). \qquad (6)$$

MATLAB® robust regression with a bisquare weight function was used to fit Eq. (6) to n obtained from the model simulations with the different identification criteria. This yields proportionality parameters, β_c (Fig. 2b). The values of β_c are approximately constant for a range of criteria sets. Robust averaging of β_c (average excluding the maximum and minimum 25% of a data sample) yields $\beta = 5.8 \text{ km}^{-2} \text{ h}^{-1}$.

5. Dust devil properties

DD intensity varies strongly from case to case, but is in general dependent on the background atmospheric state. Fig. 3a–c shows
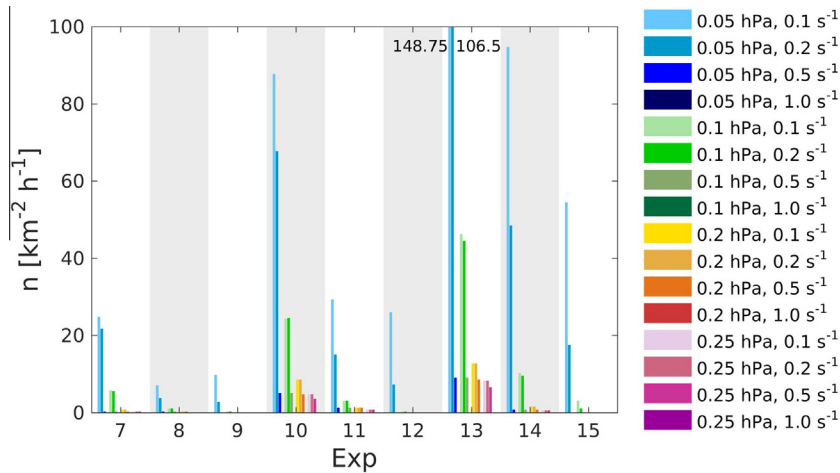

Fig. 1. (a) Histogram of DD number density, n [km^{-2} h^{-1}], at 10 m height for Exp 7–15, obtained using the identification criteria listed in the legend.

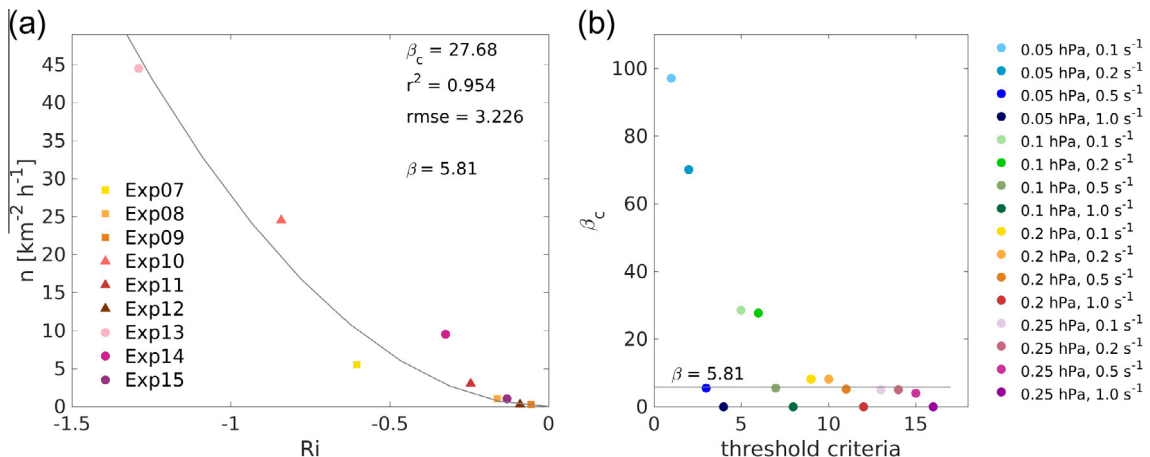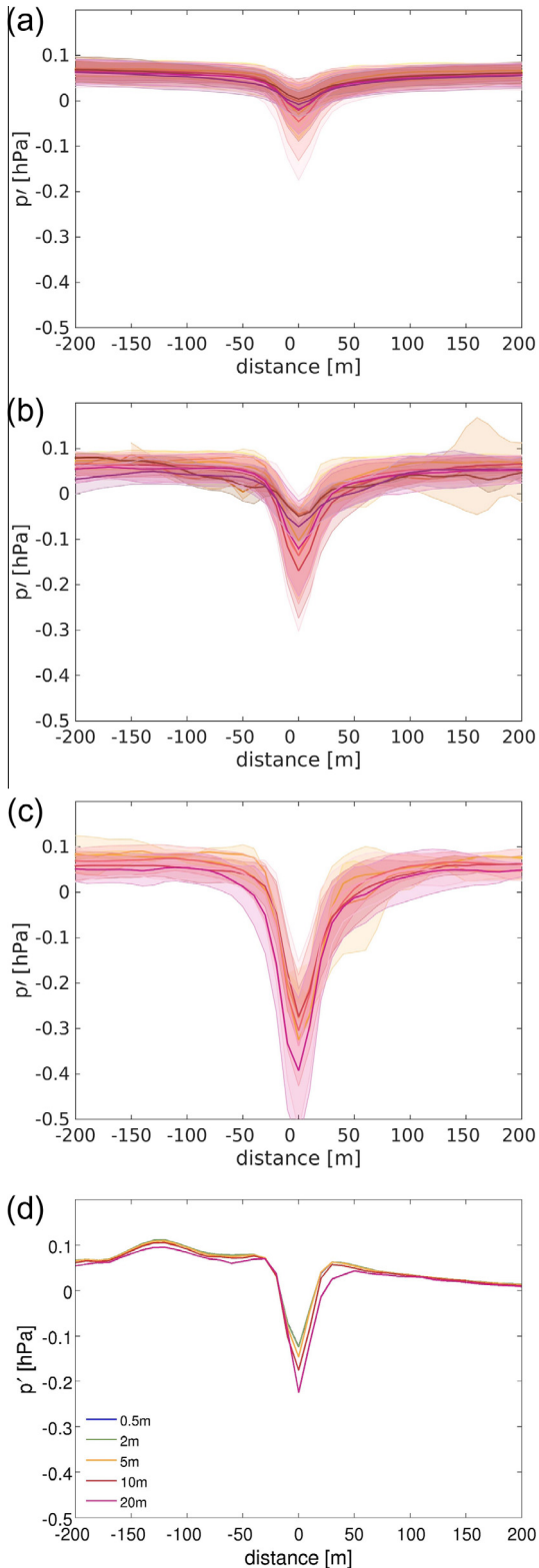**Fig. 2.** (a) DD counts, N, detected with $\Delta p_t = 0.1$ hPa and $\zeta_t = 0.2$ s^{-1} versus Richardson number for 10 m height; (b) Proportionality factors, β_c, obtained from the fit in (a) for the different detection criteria and robust average, β, used in Eq. (6).

Fig. 3. Mean cross section of pressure deviation from horizontal mean averaged over all DDs per experiment at 10 m height. Shadings indicate standard deviations. The top panels show results obtained with different identification criteria: (a) $\Delta p_t = 0.05$ hPa, $\zeta_t = 0.1$ $^{-1}$, (b) $\Delta p_t = 0.1$ hPa, $\zeta_t = 0.2$ $^{-1}$, and (c) $\Delta p_t = 0.2$ hPa, $\zeta_t = 0.5$ $^{-1}$; (d) shows an example of pressure deviation at different heights in a DD detected in Exp13.

composite cross sections of Δp, averaged over all DDs detected in a particular experiment for three combinations of identification criteria. For an individual DD, the cross section is obtained as the

mean value of x- and y-cross sections through the DD center. The average pressure drop, $\langle \Delta p \rangle$, increases with Δp_t as a larger threshold constrains detections to DDs with large pressure drops. A similar observation can be made for increasing ζ_t (Fig. 4a).

A comparison of the cross sections between the experiments shows that the maximum $\langle \Delta p \rangle$ occurs at the conditions most favorable for DD formation, i.e. strong instability and weak wind shear. This can be best recognized for small Δp_t and ζ_t (Fig. 3a) as the corresponding results include the largest number of vortices. The maximum Δp found is 1.14 hPa for a DD in Exp13. Fig. 3d shows an example of pressure deviation through an individual DD for 5 vertical levels. In general, Δp typically increases with height in the lowest levels, but for many cases varies hardly. Consequently, the average pressure cross sections do not differ significantly between the lowest levels.

Fig. 4a–c shows vorticity, ζ, turbulent vertical wind speed, $w' = w$ (as $\overline{w} \approx 0$), and DD duration, τ, versus Δp at 10 m height. Shown are the maximum values occurring during the lifetime of a DD. Vorticity is found to increase with $\sqrt{\Delta p}$, confirming the causal relationship between DD rotation and pressure drop, i.e. the vortex being close to cyclostrophic balance (Greeley et al., 2003. This suggests that using either Δp_t or ζ_t is sufficient as criterium for DD identification. If both criteria are used, they should be chosen consistently (see also Section 4). Large vorticities are only found for the most unstable cases (Exp10 and Exp13). Exp14 shows occasionally large vorticities.

The maximum turbulent vertical wind speeds, w', vary between 0.5 and 6 m s^{-1} (Fig. 4b). The maximum turbulent horizontal wind, $u'_h = \sqrt{u'^2 + v'^2}$, ranges between 2 and 10 m s^{-1} and increases with Δp (not shown). Both w' and u'_h were calculated within a box of $(i \pm 25, j \pm 25)$ around the DD center (i,j) for the height level considered to allow for the detection of the maximum velocities associated with the DD. The box size was chosen such that even the DDs with the largest diameters found fit into the box. The largest values of w' are found for Exp10 and Exp13, followed by Exp11 and Exp14.

DD duration, τ, generally increases with Δp, but with large scatter (Fig. 4c). Most DDs have relatively short durations of ~ 1 min. Durations longer than ~ 2 min are found in Exp7, 10, and 13 for DDs with diameters $d \approx 50$ m. This peak may be related to the spatial resolution of 10 m, which constrains the detection of DDs with diameters smaller than 20–40 m. We define d as the width at $0.5\Delta p$ (see Fig. 3d). This definition is analogous to the concept of full width at half maximum and is also supported by analytical models, which often assume that pressure at the vortex wall is half that in the vortex center (Lorenz et al., 2015). d is obtained through cubic spline interpolation. We use Δp rather than maximum tangential wind speed to define d, as the latter is more difficult to determine through interpolation. No close relationship between τ and d is found, but τ is generally shorter for larger d and stronger winds (Fig. 4d). For the 10 m level, the ensemble means ($\pm$standard deviations) are $\langle d \rangle = 86 \pm 33$ m and $\langle \tau \rangle = 1.05 \pm 0.83$ min. A table listing more detailed statistics obtained for d, τ, and Δp from Exp7-15 is provided as Supplementary material.

In field experiments, Lorenz et al. (2015) measured pressure drops lower than 1.6 hPa using an array of pressure loggers at fixed locations. Sinclair (1973) recorded larger pressure drops of $\sim 2.5-4.5$ hPa using instruments mounted on a vehicle to measure the properties inside selected DDs which are typically exceptionally large and long-lived. Mason et al. (2014) also used a vehicle encounter approach, but only measured pressure drops smaller than 0.5 hPa. Observed maximum vertical wind speeds in DDs were reported to be below 7 m s^{-1} by Metzger et al. (2011) and below 10 m s^{-1} by Sinclair (1973) and Renno et al. (2004). Ryan and Carroll (1970) measured wind speeds below ~ 2 m s^{-1}. Most
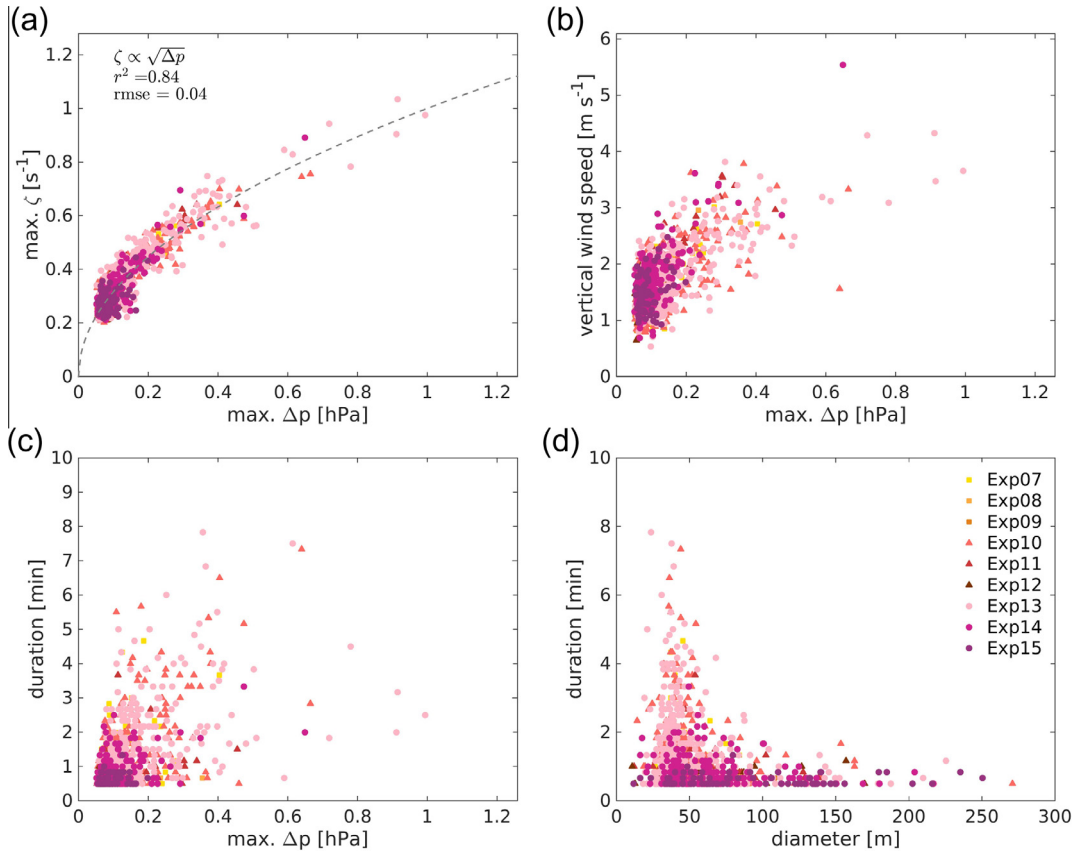
Fig. 4. Scatter plots showing (a) maximum vorticity ζ, (b) maximum vertical wind speed w', and (c) DD duration τ vs. maximum pressure drop Δp; (d) shows DD diameter d vs. τ. Colors denote the LES experiments (Table 1). Results are shown for DDs detected with $\Delta p_t = 0.05$ hPa and $\zeta_t = 0.2$ s^{-1} at 10 m height.

observed DDs are smaller than 30 m (Sinclair, 1969) or 100 m (Snow and McClelland, 1990) in diameter and typically last only few minutes (Sinclair, 1969; Snow and McClelland, 1990; Balme and Greeley, 2006). In our study, pressure drops are below ~ 1 hPa, maximum vertical wind speeds in the range of 0.5–6 m s^{-1}, diameters smaller than ~ 300 m, but mostly below 100 m, and DD durations are typically shorter than 2 min with a maximum of about 8 min. Although the number of small DDs ($d < 20$ m) is likely an underestimation in our study, our LES experiments produced DDs with properties in good agreement with field observations and thus provide a basis for quantifying DD dust transport.

6. Dust devil dust entrainment

Fig. 5 shows an example of PM20 (particulate matter with diameter < 20 μm) dust concentration and dust emission in a DD in Exp10. The maximum dust concentration occurs in the DD center and coincides with the maximum Δp. Maximum dust emissions occur around the DD center where the shear stress is strongest. Previous studies (e.g. Klose et al., 2014; Li et al., 2014) suggested that CTDE is usually of the order of magnitude $10^0 - 10^1$ μg m^{-2} s^{-1}, 1–2 orders of magnitude smaller than the typical dust emission due to saltation bombardment (e.g. Shao et al., 2011). The analyses here show that in strong DDs, turbulent dust emission can be as large as 10^3 μg m^{-2} s^{-1} which is comparable to the typical order of magnitude of dust emission caused by saltation bombardment.

As dust emission varies across a DD, dust emission in the DD center is not representative. We thus calculate the average DD dust emission, F, over an area $\sigma = \pi d^2$ at a given time. A circle with
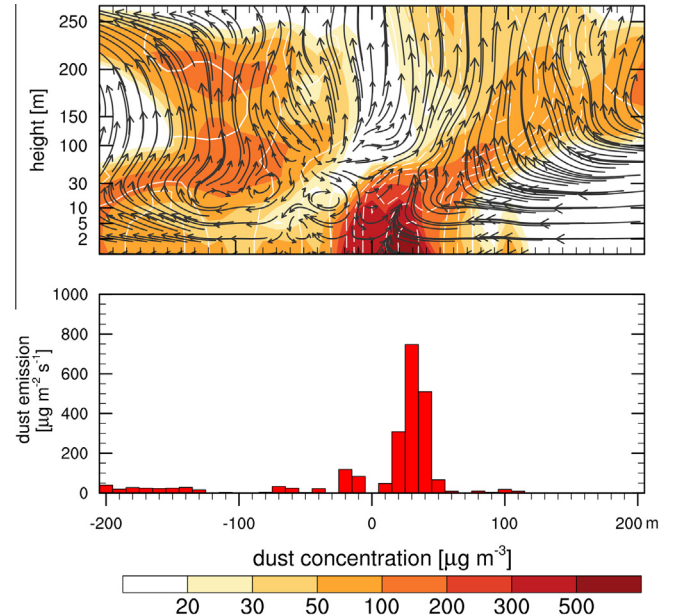
Fig. 5. (Top) Vertical cross section of PM20 dust concentration (shaded), perturbation pressure (contour lines), and wind vectors through a DD in Exp10; (Bottom) linear cross section of PM20 dust emission corresponding to the top plot.

diameter $2d$ is chosen here to make sure that the maximum shear stresses and associated maximum dust emissions occur within the averaging area. Fig. 6a shows F at the time of maximum Δp versus Richardson number, Ri. Ri is not constant for a given experiment,
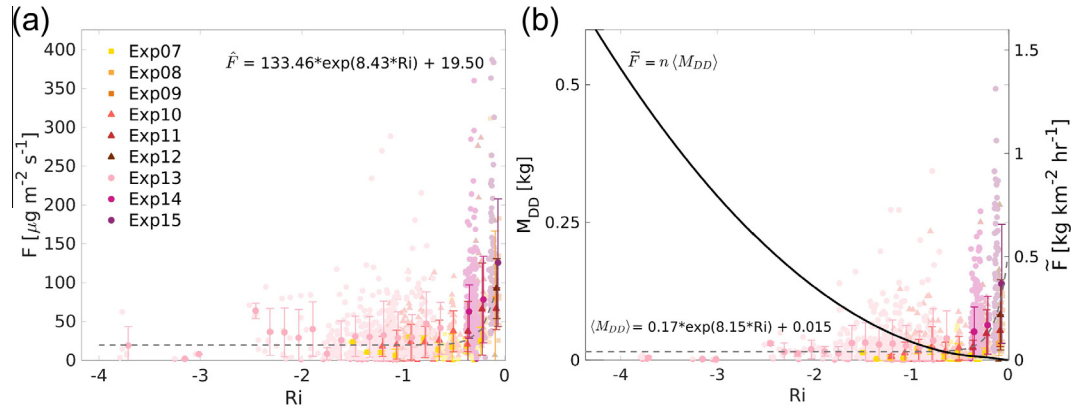
Fig. 6. (a) Dust emission F [μg m^{-2} s^{-1}] and (b) emitted dust mass M_{DD} (dashed line) together with the flux estimate $\widetilde{F}$ according to Eqs. 10 and 11 (solid line). The plots show results obtained for individual DDs detected at 10 m height with $\Delta p_t = 0.05$ hPa and $\zeta_t = 0.2$ s^{-1} (shaded) and averages over Ri-bins (unshaded) with error bars illustrating the standard deviations.

but varies, as u_* varies with time. The results show that F varies strongly for a given atmospheric stability, but the maximum values are constrained by stability to a limiting envelope, a result consistent with those of Mason et al. (2014) and Lorenz and Jackson (2015), who measured solar attenuation in DDs as indicator for dust loading. The variability in F exists even without the variation in surface dust supply which is a determining factor under natural conditions. Mean values of F are calculated for Ri bins of varying width, $\widehat{F}_{bin}$, and are shown with the corresponding standard deviations for a bin width of 0.14 in Fig. 6a. A functional relationship for $\widehat{F}_{bin}$ is obtained with robust curve fitting using a bisquare weight function for different bin-widths. The resulting coefficients are then averaged to obtain a relationship for $\widehat{F}$, which is independent of bin width. Dust emission $\widehat{F}$ [μg m^{-2} s^{-1}] is found to increase exponentially with Ri as

$$\widehat{F} = \begin{cases} 133.5 \times \exp(8.4 Ri_{10m}) + 19.5 & \text{for } Ri_{10m} < 0 \\ 0 & \text{otherwise}. \end{cases} \quad (7)$$

The inclusion of dust emission in WRF/LES-D offers the possibility to statistically analyze the dust carried by DDs. The dust mass emitted by an individual DD during its livetime τ is

$$M_{DD} = \int_0^\tau F(t)\sigma(t)\mathrm{d}t \quad (8)$$

and the ensemble average of emitted dust mass is

$$\langle M_{DD} \rangle = \frac{1}{N} \sum_{i=1}^N M_{DD}. \quad (9)$$

The average DD dust emission per unit area and unit time, $\widetilde{F}$, is then

$$\widetilde{F} = \frac{N}{AT} \langle M_{DD} \rangle = n\langle M_{DD} \rangle. \quad (10)$$

Robust curve fitting for different bin widths yields on average

$$\langle M_{DD} \rangle = \begin{cases} 0.17 \times \exp(8.15 Ri) + 0.015 & \text{for } Ri < 0 \\ 0 & \text{otherwise}. \end{cases} \quad (11)$$

with $\langle M_{DD} \rangle$ in [kg] (Fig. 6b). The DD dust flux as obtained with Eq. (10) together with Eq. (11) is shown in Fig. 6b. Using these relationships, $\widetilde{F}$ can now be readily estimated from large-scale model data (Section 7).

7. Regional estimate of dust devil occurrence and dust transport

Eqs. (6), (10), and (11) were applied to regional modeling results to estimate DD occurrence and dust transport on a larger scale.

Klose (2014) conducted model simulations for Australia using the Advanced Research WRF Version 3.51 with coupled chemistry (WRF-Chem) in regional mode for a time period of one year (July 2007–June 2008). The model was run at a 30 km horizontal resolution and used 39 vertical layers up to the 50 hPa pressure level. Consecutive model runs of 3.5 days length were conducted, which were set up to overlap by 12 h so that the first half day of each simulation could be used for model spin up and is not used for analysis. The length of the last simulation in each month depended on the number of days in that month and thus varied from 2.5 to 4.5 days. This procedure has been chosen to achieve a good accuracy of the meteorological parameters with at the same time a relatively small number of simulations. Six-hourly NCEP (National Centers for Environmental Prediction) Final Analysis (FNL) data at 1° horizontal resolution were used as model initial and boundary conditions. Model results were output every hour. For more details on the model settings, see Klose (2014).

Richardson number, Ri, was calculated from the simulations based on Businger et al. (1971) for 10 m height. Vegetation cover, σ, was not included in the LES described earlier and is thus not accounted for in Eq. (6). In general, DD occurrence is inversely proportional to vegetation cover, although small cover fractions do not preclude and may even enhance DD development (Balme and Greeley, 2006; Oke et al., 2007; Neakrase and Greeley, 2010). We thus apply a correction to Eq. (6) and calculate the number of DDs by including the effect of vegetation cover, N_σ, as

$$N_\sigma = N(1-\sigma). \quad (12)$$

Additionally, areas with large cover fractions are assumed to have no dust emissions, so N_σ is only computed for areas with $\sigma < 50\%$.

Fig. 7 shows monthly DD number density in Australia from July 2007 to June 2008. Without vegetation correction, 100–200 DDs km^{-2} mon^{-1} are predicted for wide parts of central Australia from October to March. Up to 500 km^{-2} mon^{-1} are predicted for western Western Australia (WA; Pilbara, Carnarvon, and Great Sandy Desert), for an area stretching from eastern South Australia (SA) to western New South Wales (NSW), and for southern Northern Territory (NT) in May. After accounting for vegetation cover, Eq. (12) generates smaller numbers of up to 200 km^{-2} mon^{-1} in central Australia and up to 300 km^{-2} mon^{-1} at few locations in the aforementioned areas. Particular points in eastern SA (Broken Hill Complex), southern NT (Simpson Strzelecki Dunefields) and western WA (Great Sandy Desert) show occasional values of more than 500 DDs km^{-2} mon^{-1}. During the whole year of simulation the calculated DD numbers with vegetation correction sum up to about 900–1000 DDs per year in the areas of predicted high occurrence frequency (western WA, eastern SA, and western NSW) and reach
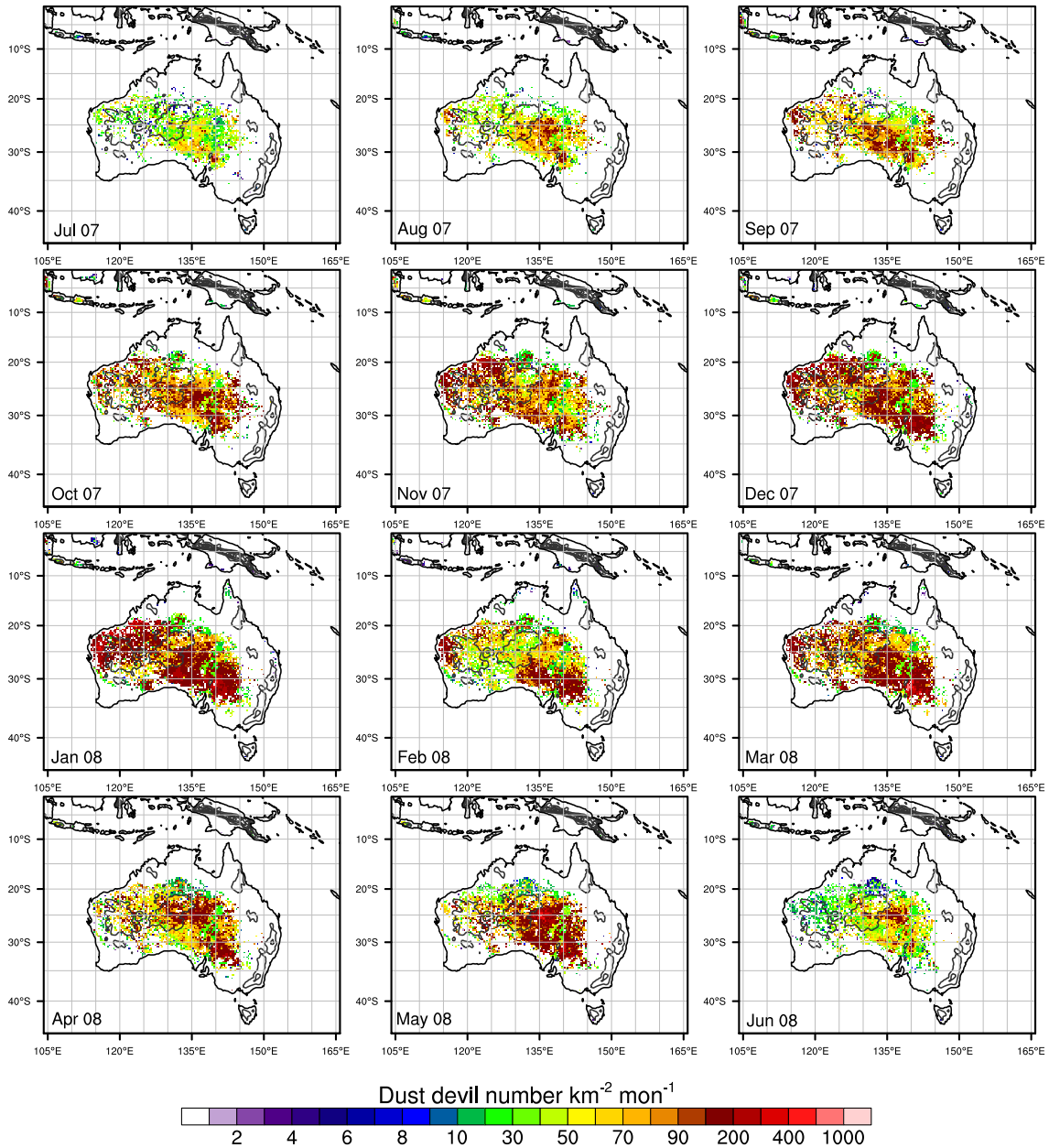
Fig. 7. Predicted monthly number of DDs per km^{-2} in Australia from July 2007 – June 2008 based on Eqs. (6) and (12).

a maximum of ~ 4000 km^{-2} yr^{-1} at Broken Hill Complex (Klose et al., 2016).

In other studies, DD frequency was related to near-surface lapse rate (e.g. Ryan, 1972; Oke et al., 2007; Ansmann et al., 2009; Jemmett-Smith et al., 2015). For example, Oke et al. (2007) observed that DD activity began at a minimum lapse rate of ~ 1 K m^{-1}. Ansmann et al. (2009) found that lapse rates of 8.5–10 K m^{-1} between the surface and 2 m height were required before convective plumes developed. If we calculate N_σ only if a minimum lapse rate of 1 K m^{-1} is exceeded, we find negligible difference in our results. When applying a minimum lapse rate of 8.5 K m^{-1}, the number of DDs with lapse rate criterion, N_L, is smaller (Appendix A).

In a DD census conducted at Fowlers Gap Arid Zone research station in western NSW (31°S 142°E), Oke et al. (2007) counted 557 DDs during 20 observation days in a 35 km^2 area, equivalent to about 25 km^{-2} mon^{-1}. The census was conducted in January 2001. For January 2008, our approach suggests $N_\sigma \approx 32$ km^{-2} mon^{-1} in

the corresponding area without or $N_L \approx 5$ km^{-2} mon^{-1} with lapse rate criterion, so our estimates are plausible. Both N_σ and N_L are larger in the surrounding of the grid cell corresponding to the Fowlers Gap research station. A case-based comparison would be required to further validate our estimates. No size estimate for the observed DDs is given by Oke et al. (2007).

When using N_σ as the number of DDs, Eqs. (10) and (11) produce DD dust emissions of 1–3 kg km^{-2} mon^{-1} in most regions in central Australia and up to 6 kg km^{-2} mon^{-1} in parts of WA and the SA/NSW belt identified earlier, with only few points exceeding 6 kg km^{-2} mon^{-1} (Fig. 8). The largest values of more than 10 kg km^{-2} mon^{-1} are found in the Great Sandy Desert in January 2008 and at Broken Hill Complex in March 2008. Using N_L instead of N_σ as the basis for calculating dust transport reduces DD dust emissions due to smaller DD numbers (Appendix A).

During the whole year, a total of 0.11, 0.07, or 0.02 Tg yr^{-1} of dust (PM20) was emitted by DDs when using respectively N, N_σ,
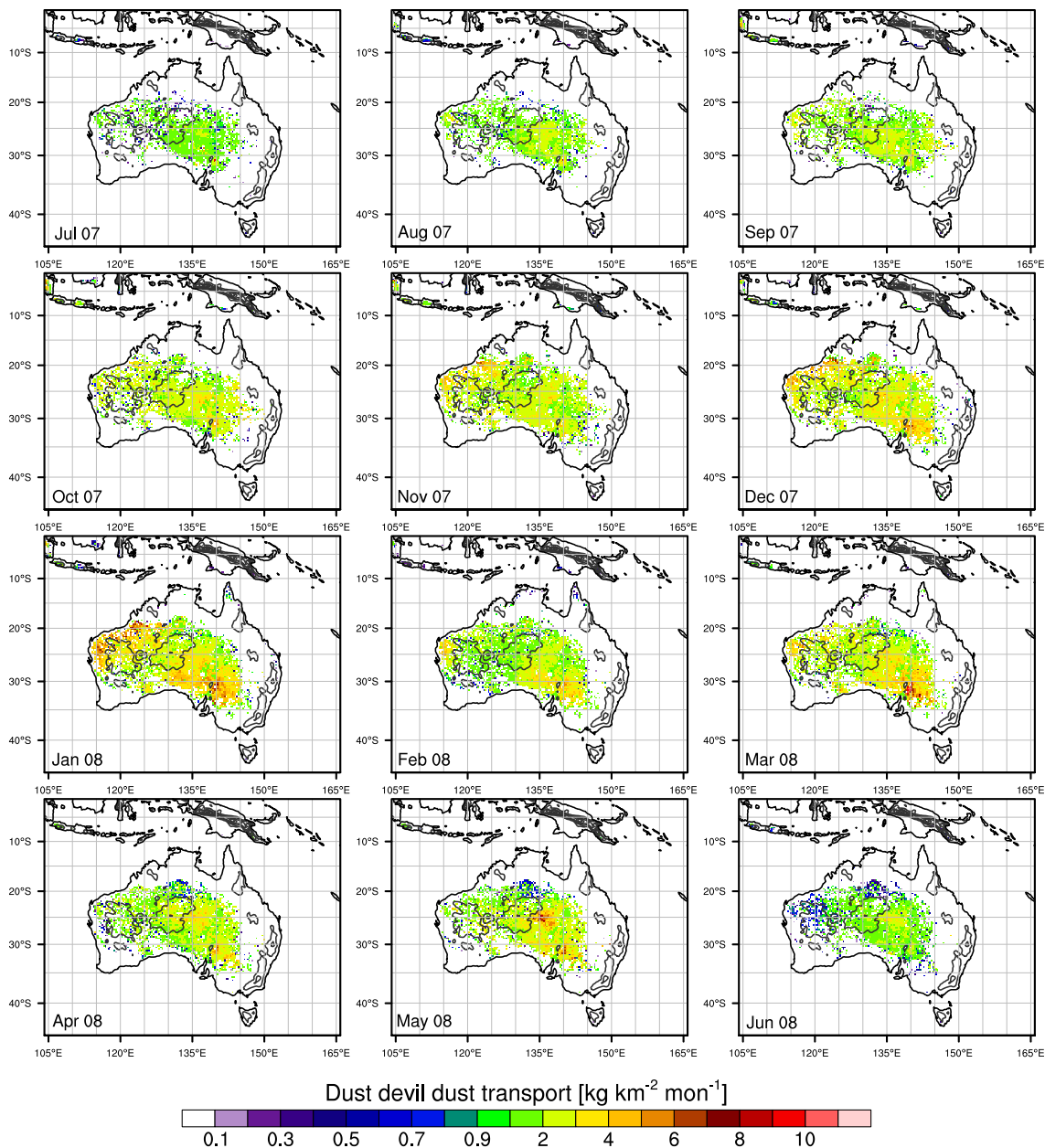
Fig. 8. Predicted monthly DD dust flux in Australia from July 2007 – June 2008. The DD number density is based on Eqs. (6) and (12) and the corresponding DD dust flux is obtained with Eqs. (10) and (11).

or N_L. The estimates of total annual dust emissions for Australia vary significantly (Huneeus et al., 2011; Shao et al., 2011, and references therein). For example, estimates in the PM10 size range vary from 35.4 to 132 Tg yr^{-1} (average 71 Tg yr^{-1}, standard deviation 36 Tg yr^{-1}) (Luo et al., 2003; Zender et al., 2003; Huneeus et al., 2011). In the PM20 size range, models predictions range from 14.9 to 106 Tg yr^{-1} (average 59 Tg yr^{-1}, standard deviation 37 Tg yr^{-1}) (Tanaka and Chiba, 2006; Huneeus et al., 2011). Assuming annual dust emissions of 59 Tg yr^{-1}, the contribution of DDs to the total dust emission would be 0.19, 0.12, and 0.03% for N, N_σ, and N_L. The contribution of DDs with diameters too small to be detected in our study may increase the overall DD dust emission due to their higher occurrence frequency compared to large DDs. However, it is unlikely that the inclusion of small DDs would increase the overall DD dust emission to more than few percent. The dust emissions for individual DDs obtained in our study are smaller or on the lower end of those obtained in the field as only

aerodynamic entrainment is considered in our model and also because dust emissions were calculated for a loam soil. Using a clay soil in our model would produce larger dust fluxes. However, if dust emissions were increased by one or two orders of magnitude, then the DD contribution would still be in the range of ~0.3–19%. On the other hand, the abundance of dust particles available for lifting is often limited due to crusting or stone cover, which is not accounted for in the model. This would again decrease the DD contribution to the total dust budget.

8. Discussion and conclusions

In this paper, dust devil (DD) dust transport was investigated using LES. Our results show that the DD number density, n, decreases with Ri^2 for negative Ri. n is smaller in our study than in the studies of Ohno and Takemi (2010) and Raasch and Franke
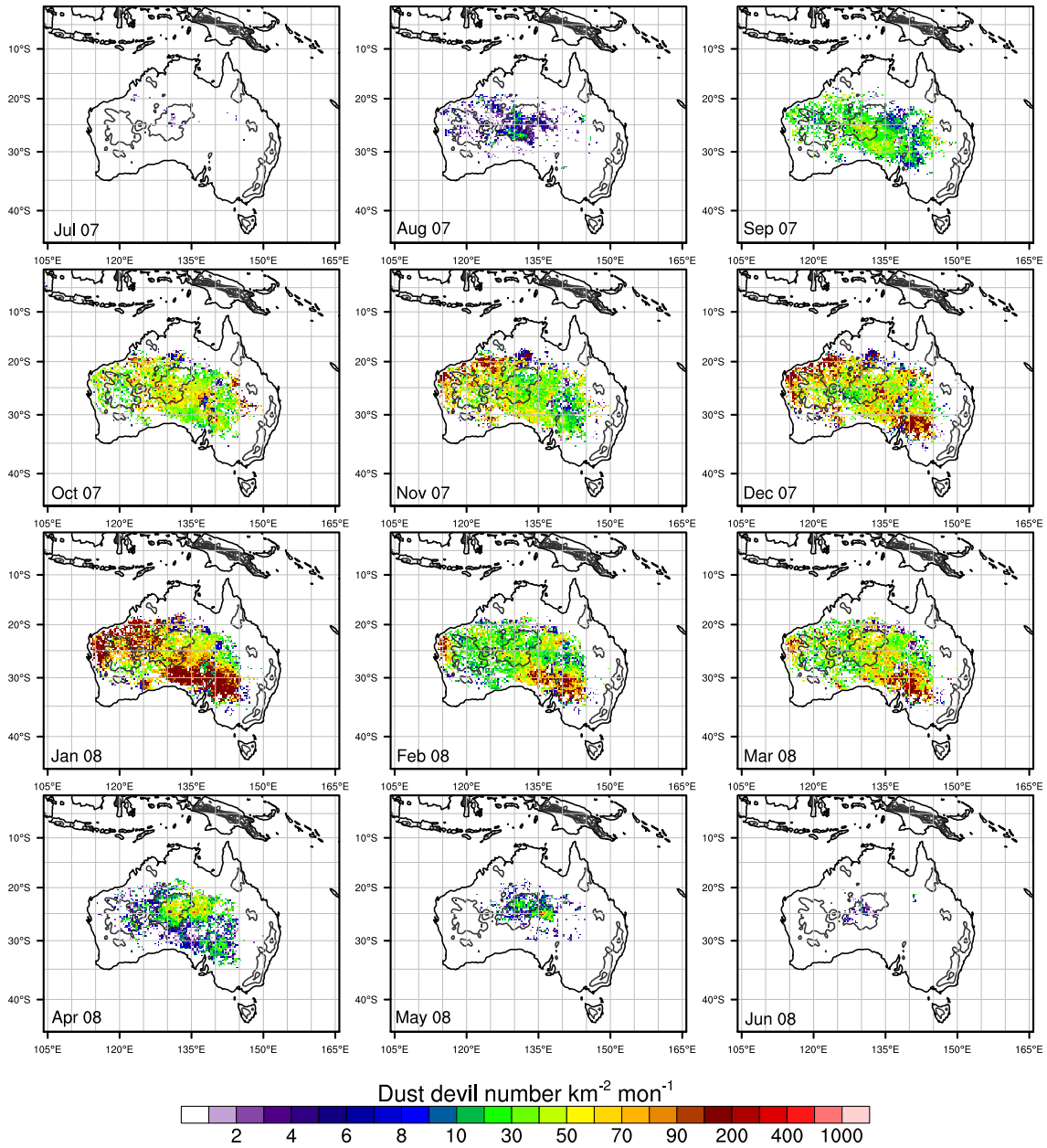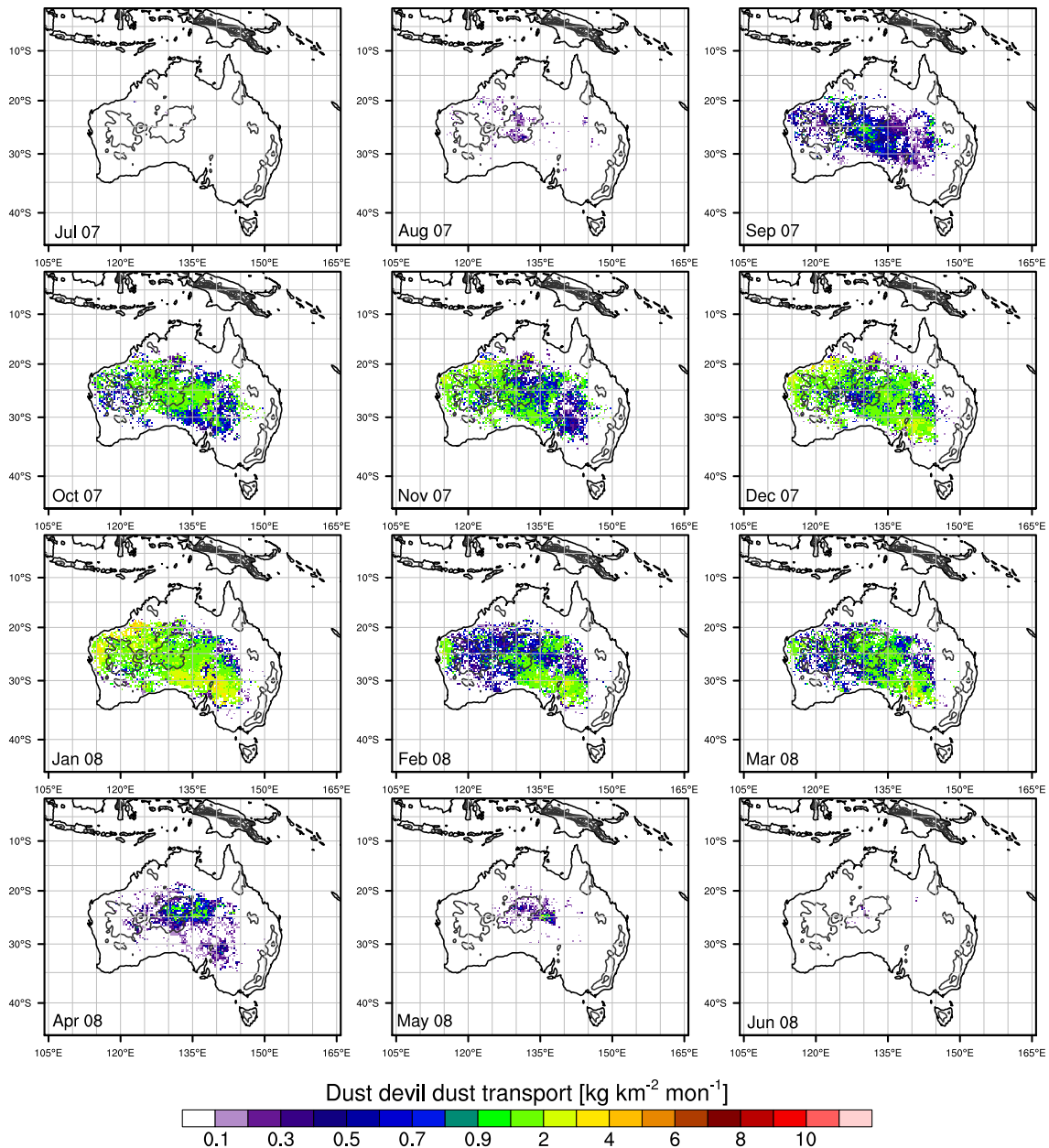
Fig. A.9. Monthly number of DDs occurring in Australia from July 2007 – June 2008 calculated based on Eqs. (6) and (12), but only if the lapse rate between surface and 2 m temperature exceeded 8.5 K m^{-1}.

(2011). The reason is likely the higher horizontal resolution used in the latter studies. For example, Raasch and Franke (2011) identified twice as many DDs when using a 1 m horizontal resolution in their simulations rather than a 2 m grid resolution. Additionally, we excluded short tracks and connected tracks if pressure minima were found in the intermediate locations, thereby reducing our n.

The order of magnitude of pressure drop, turbulent wind speed, and duration of the detected DDs are in agreement with those observed in the field (e.g. Sinclair, 1969; Metzger et al., 2011; Lorenz et al., 2015). With a mean value of $\langle d \rangle = 86$ m, the diameters in our study are somewhat larger than that of observed DDs (Balme and Greeley, 2006; Lorenz, 2011), with one reason likely being the different definition used to determine DD diameter. Another reason is probably an underestimation of the number of small DDs in our study.

Our results show that instantaneous shear stresses in DDs are sufficiently large to aerodynamically lift dust particles as has been observed by Balme et al. (2003). Surface dust fluxes of about $10^0 - 10^3$ µg m^{-2} s^{-1} and 2 m PM20 dust concentrations of $10^0 - 10^3$ µg m^{-3} have been obtained in our study, smaller or on the lower end of those observed in laboratory experiments and in the field. Neakrase and Greeley (2010) measured total mass removals of $10^5 - 10^{11}$ µg m^{-2} s^{-1} for 2 µm clay in their laboratory vortex generator experiments, much larger than the fluxes obtained here. In the field, Metzger et al. (2011) measured PM10 concentrations of $10^3 - 10^4$ µg m^{-3} at 2 m height, close to those obtained in our study for the more intensive DDs. Renno et al. (2004) report concentrations of about 10^5 µg m^{-3} in strong dust plumes and DDs. Dust emission fluxes in our study are surface fluxes and are thus not directly comparable with the fluxes estimated by Renno et al. (2004) and Metzger et al. (2011). Fluxes at a height above the surface are likely larger due to convergence toward the DD center. Also, strong DDs are probably more often

Fig. A.10. Monthly DDs dust flux occurring in Australia from July 2007 – June 2008. The DD number density is based on Eqs. (6) and (12), but only if the lapse rate between surface and 2 m temperature exceeded 8.5 K m^{-1}, and the corresponding DD dust flux is obtained with Eqs. (10) and (11).

sampled in the field than less intensive ones. Furthermore, lower dust fluxes in our study are not surprising as only aerodynamic entrainment is accounted for in our parameterization. In a natural environment, intermittent saltation leads to additional dust emission (e.g. Metzger et al., 2011), which is not yet included in our model. Pressure effects might further enhance dust entrainment (Balme and Hagermann, 2006), but are partly considered in our model assuming a relationship between vertical and horizontal pressure drop in DDs. This again is directly related to vortex velocity and thus included in the lifting force in our model. The LES experiments have shown that large parts of DD dust lifting can be explained by turbulent dust emission, even if a moderately emitting loam soil is used as the surface condition.

The inclusion of a turbulent dust emission scheme in the LES model allows for the first time to investigate of DD dust transport based on surface dust emission fluxes. The statistical analysis of the simulated DD dust emission yielded a new method to estimate DD dust transport from global model data, thereby allowing to assess the relevance of DDs in the global dust cycle and to study their impact on climate and environment. Applying the new method to results of regional model simulations for Australia suggests that DDs are unlikely to contribute largely to the total dust budget on continental or global scale. However, DDs can be important in areas that show above-average DD numbers. Due to their frequent occurrence especially in summer, DDs can become a major dust event type in such regions.

Acknowledgments

Appendix A. Regional estimate of dust devil occurrence and transport with additional lapse rate criterion

Fig. A.9 shows the number of DDs when using N_L, i.e. calculating N_σ (Eq. 12) only if the lapse rate between surface and 2 m temperature exceeds 8.5 K m^{-1}. Compared to N_σ, N_L reduces the number of DDs to 30–50 km^{-2} mon^{-1} in most regions from September to March (Fig. A.9). About 100 DDs km^{-2} mon^{-1} are predicted for the high-occurrence regions in WA and SA/NSW during December to March. Maximum values of ~ 400 km^{-2} mon^{-1} are still found in the Great Sandy Desert and Broken Hill Complex areas. Based on N_L, barely any DDs occurred in winter (July–August 2007 and April–June 2008). For the whole year of simulation, N_L is mostly below 400 km^{-2} yr^{-1} and reaches maxima of about 1000 km^{-2} yr^{-1} in the high-occurrence regions in WA and Broken Hill Complex.

Fig. A.10 shows the DD dust flux obtained with Eqs. (10) and (11) in combination with N_L. Dust emissions are mostly below 2 kg km^{-2} mon^{-1} and are smaller than those predicted using N_σ. DD numbers and dust fluxes for the whole year of simulation are shown in Klose et al. (2016).

Appendix B. Supplementary data

Supplementary data associated with this article can be found, in the online version, at http://dx.doi.org/10.1016/j.aeolia.2016.05.003.

References

Ansmann, A., Tesche, M., Knippertz, P., Bierwirth, E., Althausen, D., Müller, D., Schulz, O., 2009. Vertical profiling of convective dust plumes in southern morocco during SAMUM. Tellus 61B, 340–353. http://dx.doi.org/10.1111/j.1600-0889.2008.00384.x.

Balme, M., Greeley, R., 2006. Dust devils on Earth and Mars. Rev. Geophys. 44. http://dx.doi.org/10.1029/2005RG000188.

Balme, M., Hagermann, A., 2006. Particle lifting at the soil-air interface by atmospheric pressure excursions in dust devils. Geophys. Res. Lett. 33, 3–7. http://dx.doi.org/10.1029/2006GL026819.

Balme, M., Metzger, S., Towner, M., Ringrose, T., Greeley, R., Iversen, J., 2003. Friction wind speeds in dust devils: a field study. Geophys. Res. Lett. 30, 1830. http://dx.doi.org/10.1029/2003GL017493.

Businger, J.A., Wyngaard, J.C., Izumi, Y., Bradley, E.F., 1971. Flux-profile relationships in the atmospheric surface layer. J. Atmos. Sci. 28, 181–189. http://dx.doi.org/10.1175/1520-0469(1971) 028<0181:FPRITA>2.0.CO;2.

Deardorff, J.W., 1970. A numerical study of three-dimensional turbulent channel flow at large reynolds numbers. J. Fluid Mech. 41, 453–480. http://dx.doi.org/10.1017/S0022112070000691.

Greeley, R., Balme, M.R., Iversen, J.D., Metzger, S., Mickelson, R., Phoreman, J., White, B., 2003. Martian dust devils: laboratory simulations of particle threshold. J. Geophys. Res. 108. http://dx.doi.org/10.1029/2002JE001987.

Gu, Z., Qiu, J., Zhao, Y., Li, Y., 2008. Simulation of terrestrial dust devil patterns. Adv. Atmos. Sci. 25, 31–42. http://dx.doi.org/10.1007/s00376-008-0031-7.

Huneeus, N., Schulz, M., Balkanski, Y., Griesfeller, J., Prospero, J., Kinne, S., Bauer, S., Boucher, O., Chin, M., Dentener, F., Diehl, T., Easter, R., Fillmore, D., Ghan, S., Ginoux, P., Grini, A., Horowitz, L., Koch, D., Krol, M.C., Landing, W., Liu, X., Mahowald, N., Miller, R., Morcrette, J.J., Myhre, G., Penner, J., Perlwitz, J., Stier, P., Takemura, T., Zender, C.S., 2011. Global dust model intercomparison in AeroCom phase I. Atmos. Chem. Phys. 11, 7781–7816. http://dx.doi.org/10.5194/acp-11-7781-2011, URL: http://www.atmos-chem-phys.net/11/7781/2011/.

Ito, J., Niino, H., Nakanishi, M., 2010. Large eddy simulation on dust suspension in a convective mixed layer. SOLA 6, 133–136. http://dx.doi.org/10.2151/sola.2010-034 133.

Jemmett-Smith, B.C., Marsham, J.H., Knippertz, P., Gilkeson, C.A., 2015. Quantifying global dust devil occurrence from meteorological analyses. Geophys. Res. Lett. 42, 1275–1282. http://dx.doi.org/10.1002/2015GL063078, URL: http://dx.doi.org/10.1002/2015GL063078.

Kanak, K.M., 2005. Numerical simulation of dust devil-scale vortices. Q. J. R. Meteorolog. Soc. 131, 1271–1292. http://dx.doi.org/10.1256/qj.03.172.

Klose, M., Jemmett-Smith, B.C., Kahanpää, H., Kahre, M., Knippertz, P., Lemmon, M. T., Lewis, S.R., Lorenz, R.D., Neakrase, L.D.V., Newman, C., Patel, M.R., Reiss, D., Spiga, A., Whelley, P.L., 2016. Dust devil sediment transport: from lab to field to global impact. Space Sci. Rev, submitted for publication.

Klose, M., Shao, Y., 2012. Stochastic parameterization of dust emission and application to convective atmospheric conditions. Atmos. Chem. Phys. 12, 7309–7320. http://dx.doi.org/10.5194/acp-12-7309-2012.

Klose, M., Shao, Y., 2013. Large-eddy simulation of turbulent dust emission. Aeolian Res. 8, 49–58. http://dx.doi.org/10.1016/j.aeolia.2012.10.010.

Klose, M., Shao, Y., Li, X.L., Zhang, H.S., Ishizuka, M., Mikami, M., Leys, J.F., 2014. Further development of a parameterization for convective turbulent dust emission and evaluation based on field observations. J. Geophys. Res. Atmos. 119, 10441–10457. http://dx.doi.org/10.1002/2014JD021688.

Klose, M.R., 2014. Convective Turbulent Dust Emission: Process, Parameterization, and Relevance in the Earth System. Universität zu Köln, Dissertation, URL: http://kups.ub.uni-koeln.de/id/eprint/5826.

Koch, J., Renno, N.O., 2005. The role of convective plumes and vortices on the global aerosol budget. Geophys. Res. Lett. 32. http://dx.doi.org/10.1029/2005GL023420.

Kurgansky, M.V., 2006. Steady-state properties and statistical distribution of atmospheric dust devils. Geophys. Res. Lett. 33. http://dx.doi.org/10.1029/2006GL026142.

Li, X.L., Klose, M., Shao, Y., Zhang, H.S., 2014. Convective turbulent dust emission (CTDE) observed over Horqin Sandy Land area and validation of a CTDE scheme. J. Geophys. Res. Atmos. 119, 9980–9992. http://dx.doi.org/10.1002/2014JD021572.

Lorenz, R., 2011. On the statistical distribution of dust devil diameters. Icarus 215, 381–390. http://dx.doi.org/10.1016/j.icarus.2011.06.005.

Lorenz, R.D., 2012. Power law distribution of pressure drops in dust devils: observation techniques and earth–mars comparison. Planet. Space Sci. 60, 370–375. http://dx.doi.org/10.1016/j.pss.2011.11.003, titan Through Time: A Workshop on Titan's Formation, Evolution and Fate..

Lorenz, R.D., 2014. Vortex encounter rates with fixed barometer stations: comparison with visual dust devil counts and large-eddy simulations. J. Atmos. Sci. 71, 4461–4472. http://dx.doi.org/10.1175/JAS-D-14-0138.1.

Lorenz, R.D., Jackson, B.K., 2015. Dust devils and dustless vortices on a desert playa observed with surface pressure and solar flux logging. GeoResJ 5, 1–11. http://dx.doi.org/10.1016/j.grj.2014.11.002.

Lorenz, R.D., Neakrase, L.D., Anderson, J.D., 2015. In-situ Measurement of Dust Devil Activity at La Jornada Experimental Range. Aeolian Research, New Mexico, USA. http://dx.doi.org/10.1016/j.aeolia.2015.01.012.

Luo, C., Mahowald, N.M., del Corral, J., 2003. Sensitivity study of meteorological parameters on mineral aerosol mobilization, transport and distribution. J. Geophys. Res. 108.

Mason, J.P., Patel, M.R., Lewis, S.R., 2014. The retrieval of optical properties from terrestrial dust devil vortices. Icarus 231, 385–393. http://dx.doi.org/10.1016/j.icarus.2013.12.013.

Metzger, S.M., Balme, M.R., Towner, M.C., Bos, B.J., Ringrose, T.J., Patel, M.R., 2011. In situ measurements of particle load and transport in dust devils. Icarus 214, 766–772. http://dx.doi.org/10.1016/j.icarus.2011.03.013.

Michaels, T.I., 2006. Numerical modeling of Mars dust devils: Albedo track generation. Geophys. Res. Lett. 33. http://dx.doi.org/10.1029/2006GL026268.

Moeng, C.H., Sullivan, P.P., 2015. Large-Eddy Simulation. In: North, G.R., Pyle, J., Zhang, F. (Eds.), Encyclopedia of Atmospheric Sciences, . second ed., vol. 4, pp. 232–240.

Neakrase, L.D.V., Greeley, R., 2010. Dust devil sediment flux on Earth and Mars: laboratory simulations. Icarus 206, 306–318. http://dx.doi.org/10.1016/j.icarus.2009.08.028, URL: http://dx.doi.org/10.1016/j.icarus.2009.08.028.

Neakrase, L.D.V., Greeley, R., 2010. Dust devils in the laboratory: effects of surface roughness on vortex dynamics. J. Geophys. Res. 115. http://dx.doi.org/10.1029/2009JE003465.

Ohno, H., Takemi, T., 2010. Mechanisms for intensification and maintenance of numerically simulated dust devils. Atmos. Sci. Let.

Oke, A.M.C., Tapper, N.J., Dunkerley, D., 2007. Willy-willies in the Australian landscape: the role of key meteorological variables and surface conditions in defining frequency and spatial characteristics. J. Arid Environ. 71, 201–215. http://dx.doi.org/10.1016/j.jaridenv.2007.03.008.

Raasch, S., Franke, T., 2011. Structure and formation of dust devil-like vortices in the atmospheric boundary layer: a high-resolution numerical study. J. Geophys. Res. 116, 1–16. http://dx.doi.org/10.1029/2011JD016010.

Renno, N.O., Abreu, V.J., Koch, J., Smith, P.H., Hartogensis, O.K., Bruin, H.A.R.D., Burose, D., Delory, G.T., Farrell, W.M., Watts, C.J., Garatuza, J., Parker, M., Carswell, A., 2004. MATADOR 2002: a pilot field experiment on convective plumes and dust devils. J. Geophys. Res. 109. http://dx.doi.org/10.1029/2003JE002219.

Renno, N.O., Burkett, M.L., Larkin, M.P., 1998. A simple thermodynamical theory for dust devils. J. Atmos. Sci. 55, 3244–3252.

Richardson, L.F., 1920. The supply of energy from and to atmospheric eddies. Proc. R. Soc. A 97, 354–373. http://dx.doi.org/10.1098/rspa.1920.0039.

Ryan, J.A., 1972. Relation of dust devil frequency and diameter to atmospheric temperature. J. Geophys. Res. 77, 7133–7137. http://dx.doi.org/10.1029/JC077i036p07133.

Ryan, J.A., Carroll, J.J., 1970. Dust devil wind velocities: mature state. J. Geophys. Res. 75, 531–541. http://dx.doi.org/10.1029/JC075i003p00531, URL: http://dx.doi.org/10.1029/JC075i003p00531.

Schmidt, H., Schumann, U., 1989. Coherent structure of the convective boundary layer derived from large-eddy simulations. J. Fluid Mech. 200, 511–562. http://dx.doi.org/10.1017/S0022112089000753.

Shao, Y., Wyrwoll, K.H., Chappell, A., Huang, J., Lin, Z., McTainsh, G.H., Mikami, M., Tanaka, T.Y., Wang, X., Yoon, S., 2011. Dust cycle: an emerging core theme in

Earth system science. Aeolian Res. 2, 181–204. http://dx.doi.org/10.1016/j.aeolia.2011.02.001.

Sinclair, P.C., 1969. General characteristics of dust devils. J. Appl. Meteor. 8, 32–45. http://dx.doi.org/10.1175/1520-0450(1969) 0080032:GCODD2.0.CO;2.

Sinclair, P.C., 1973. The lower structure of dust devils. J. Atmos. Sci. 30, 1599–1619. http://dx.doi.org/10.1175/1520-0469(1973) 030<1599:TLSODD>2.0.CO;2.

Snow, J.T., McClelland, T.M., 1990. Dust devils at White Sands Missile Range, New Mexico: 1. Temporal and spatial distributions. J. Geophys. Res. Atmos. 95, 13707–13721. http://dx.doi.org/10.1029/JD095iD09p13707.

Tanaka, T.Y., Chiba, M., 2006. A numerical study of the contributions of dust source regions to the global dust budget. Global Planet. Change 52, 88–104.

Wang, Z.T., 2016. A theoretical note on aerodynamic lifting in dust devils. Icarus 265, 79–83. http://dx.doi.org/10.1016/j.icarus.2015.10.016.

Zender, C.S., Bian, H., Newman, D., 2003. Mineral dust entrainment and deposition (DEAD) model: description and 1990s dust climatology. J. Geophys. Res. 108.

Zhao, Y.Z., Gu, Z.L., Yu, Y.Z., Ge, Y., Li, Y., Feng, X., 2004. Mechanism and large eddy simulation of dust devils. Atmos. Ocean 42, 61–84. http://dx.doi.org/10.3137/ao.420105.